

Leading Edge Aeronautics Research for NASA (LEARN)

Cooperative Gust Sensing and Suppression for Aircraft Formation Flight, Phase II

NASA Award Number: NNX14AF55A

Period of Performance: Mar 16, 2014 – Sep. 15, 2016

Summary of Research Report

Investigators:

Yu Gu (PI), Marcello Napolitano (Co-I), Jason Gross (Collaborator), West Virginia University,
Haiyang Chao (Co-I), Charlie ZhongQuan Zheng (Co-I), University of Kansas,
Matthew Rhudy (Collaborator), Pennsylvania State University, Reading.

Address: PO Box 6106, Morgantown, WV, 26506

Phone: (304) 293-3992, Email: yu.gu@mail.wvu.edu,

Technical Officer

Curtis E. Hanson

NASA Armstrong Flight Research Center

PO Box 273, MS 4840D, Edwards CA 93523-0273

Phone: (661) 276-3966, Email: curtis.e.hanson@nasa.gov

December 2016

1. Executive Summary

Autonomous formation flight is an enabling technology for many future concepts of operations involving both manned and unmanned aircraft. Its potential benefits include energy saving and improved aircraft coordination within a high density airspace. However, with the following aircraft constantly flying in the leader's wake, several technical challenges need to be overcome before commercial aircraft and Unmanned Aerial Vehicles (UAVs) can routinely and safely fly in formation. Many challenges are related to the modeling, prediction, and real-time sensing of the dynamic airflow field, which includes both ambient and wake-induced wind gust disturbances.

The objective of this overall research effort was to develop and experimentally validate a cooperative strategy for gust sensing and suppression within a close formation flight setting. During the Phase I effort, a real-time wind estimation algorithm was developed. Additionally, the concept of cooperative wind sensing was validated in simulation studies. Furthermore, autonomous close formation flights were achieved using two sub-scale research aircraft at a 5x wingspan distance. The effects of the wake vortices were successfully recorded by sensors onboard the follower aircraft.

During the Phase II effort, wake identification from UAV formation flight data was performed. An integrated aerodynamics and flight dynamic simulator for UAS wake encounters was developed using the vortex lattice method. Four different wind speed estimation algorithms were developed and compared using simulated and flight data. The research test beds were upgraded with new sensors, propulsion systems, communication devices, and newly designed avionics. Over 45 flight testing experiments were performed for supporting system integration tasks and for collecting research data. A relative navigation algorithm fusing measurements provided by a carrier phase differential GPS receiver, inertial sensors, and ranging radios was developed to improve the robustness of the navigation solution. A novel computer vision based airflow angle estimation method was also developed and validated with flight data. Each of these technical developments are presented in this report.

During the Phase II effort, five graduate students and two undergraduate students from West Virginia University (WVU) and the University of Kansas (KU) were involved. The research project has so far produced four journal and six conference publications, as listed in Appendix A.

2. Wake Identification from UAV Formation Flight Data

The WVU close-formation-flight data collected in 2013 were investigated for identifying wake encounter periods as well as for wake model identification purposes. Wake identification was first performed based on the difference of two fuselage mounted Angle of Attack (AOA) sensors, and further validated using measurements from additional sensors including rate gyroscope, accelerometer, and Angle of Sideslip (AOS) sensors.

2.1 – Flight Data Summary

A total of four formation flight data sets were used for this study with each flight lasting approximately four minutes. The leader aircraft flew in manual mode while the follower aircraft flew for approximately two minutes in autonomous mode and the other two minutes (including takeoff and landing) in manual mode. A typical flight trajectory from a single loop of formation flight is shown in Fig. 1, with the leader plotted in red and the follower plotted in green. The

trajectory included two half circles with a turning radius of 120 meters and two straight legs with the length of about 450 m. Since the Phastball UAV has a cruise speed of approximately 30 m/s, the maximum time for continuous wings level straight flight was approximately 15 seconds.

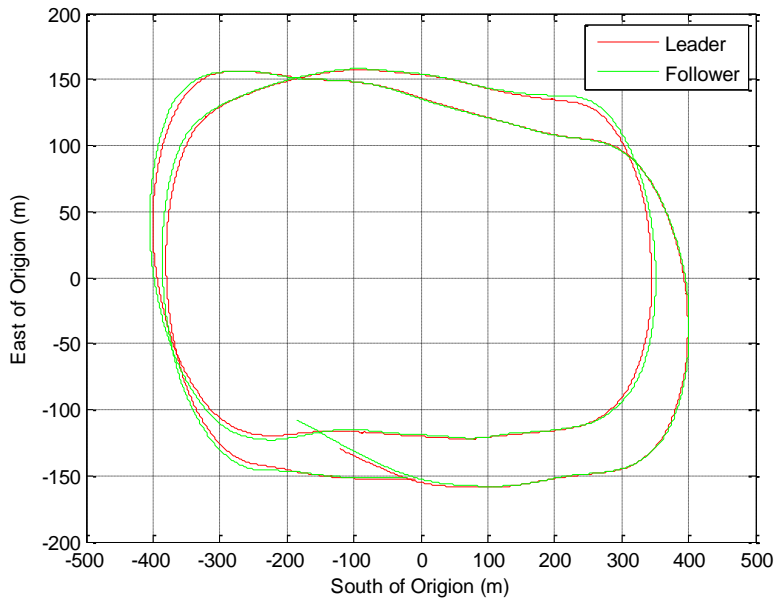


Fig. 1. Trajectory for formation flight 1.

For this particular flight, the follower UAV was commanded to maintain a 12 meter longitudinal offset from the leader, a 1.2 meter lateral offset on the left of the leader, and a zero meter vertical offset. The tracking performance from flight 1 is shown in Fig. 2. It can be observed that the tracking performance is well maintained to within a few meters during the wings level straight leg portion of the flight [1].

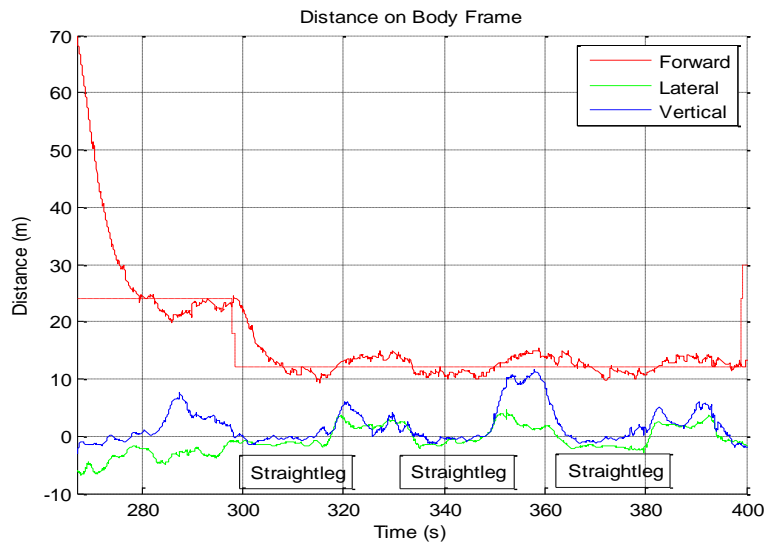


Fig. 2. Tracking performance for formation flight 1.

2.2 – Wake Encounter Identification

All wake encounter experiments in the past used manned aircraft as the leader to generate wake vortices. Most of these tests rely on 5-hole Pitot tube or other air flow sensors for a direct indication of wake encounters. In fact, it is quite challenging to identify the wake encounter from small UAV flight data due to the limitations from the onboard sensors as well as disturbances caused by ambient wind gusts. In the 2013 flight season, the Phastball UAV was equipped with two fuselage mounted AOA sensors and one fuselage mounted AOS sensor. These three air flow sensors are major indications of wake encounters. However, these air flow measurements are also corrupted with sensor noises and local gust disturbances, as shown in Fig. 3.

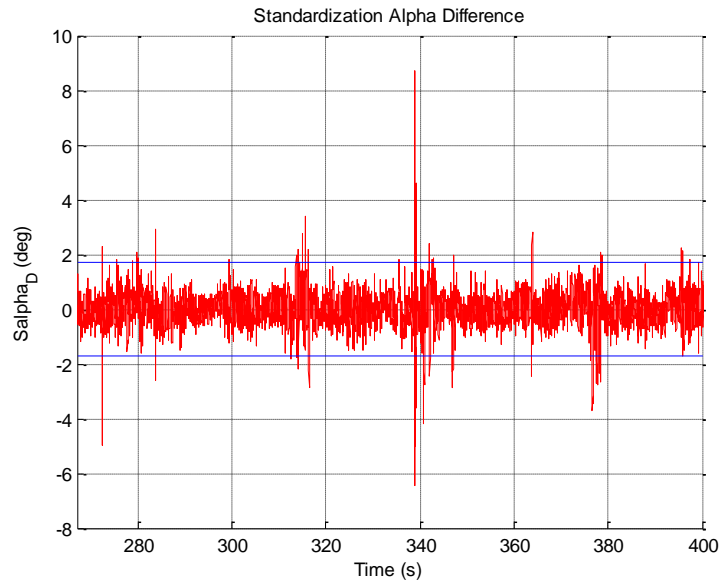


Fig. 3. Difference between left and right AOA sensors.

For the simplicity of the problem, we only focused on the wings level straight portions of the flights for wake encounter identification purposes. The difference between the left and right fuselage mounted AOA sensors is used as the indicator of wake encounter after considering the measurement noise. In other words, the wake encounter period is selected when the difference between the two AOA sensors goes out of the 3σ range of the nominal values. It can be observed from Fig. 3 that only a few cases were detected from flight 1 with the AOA difference greater than 3σ . In fact, only one of them happened during wings level straight flight.

The above wake encounter identification method is used for all four close formation flights performed on 10/12/2013. The results are shown in Table 1. Out of the four flights, wake encounters were experienced in three flights at the longitudinal offset of about 12 meters (approximately 5 wingspan). The wakes of the leader hit mostly on the left vane for the first two flights and mostly on the right vane for the last flight. The wake encountering periods varied from 0.3 to 0.6 second, which are dependent on how the follower traveled through the wake. This also indicates that the wake dimension for Phastball is fairly small, as expected.

TABLE 1 – WAKE ENCOUNTER FLIGHT SUMMARY

Flight No	Desired Geometry	Wake Hit Vane	Formation Flight Time	Wake Encounter Period
1	(12-24, -1, 0)	Left Vane	267-400 sec.	338.8-339.2 sec.
2	(12-24, -1, 0)	Left Vane	117-380 sec.	181-181.3 sec.
3	(12-24, -1, 0)	None	267-400 sec.	None
4	(12-24, -1, 0)	Right Vane	89-334 sec.	237.5-237.8 sec.
4	(12-24, -1, 0)	Right Vane	89-334 sec.	239.3-239.7 sec.

2.3 – Wake Encounter Data Example

A representative set of flight data with wake encounter detections is shown in Fig. 4. Wake encounter period is identified from wings level flight based on the difference between the left and right AOA sensors. The wake effect can also be observed from other sensors including rate gyros, AOS, and accelerometers. The following behaviors have been observed from all wake encounter flight data.

- Difference between left and right AOA measurements greater than 3σ (i.e., 1.5 deg.);
- Abrupt movements on sideslip angle sensor (> 5 deg.);
- Abrupt roll rate observed from gyro measurements (> 15 deg./sec.);
- Consequent vertical motions observed from accelerometer measurements (> 0.2 G).

The abrupt negative rolling during the wake encounter is due to the fact that the follower aircraft encounter the downdraft of the wake mostly from the left wing.

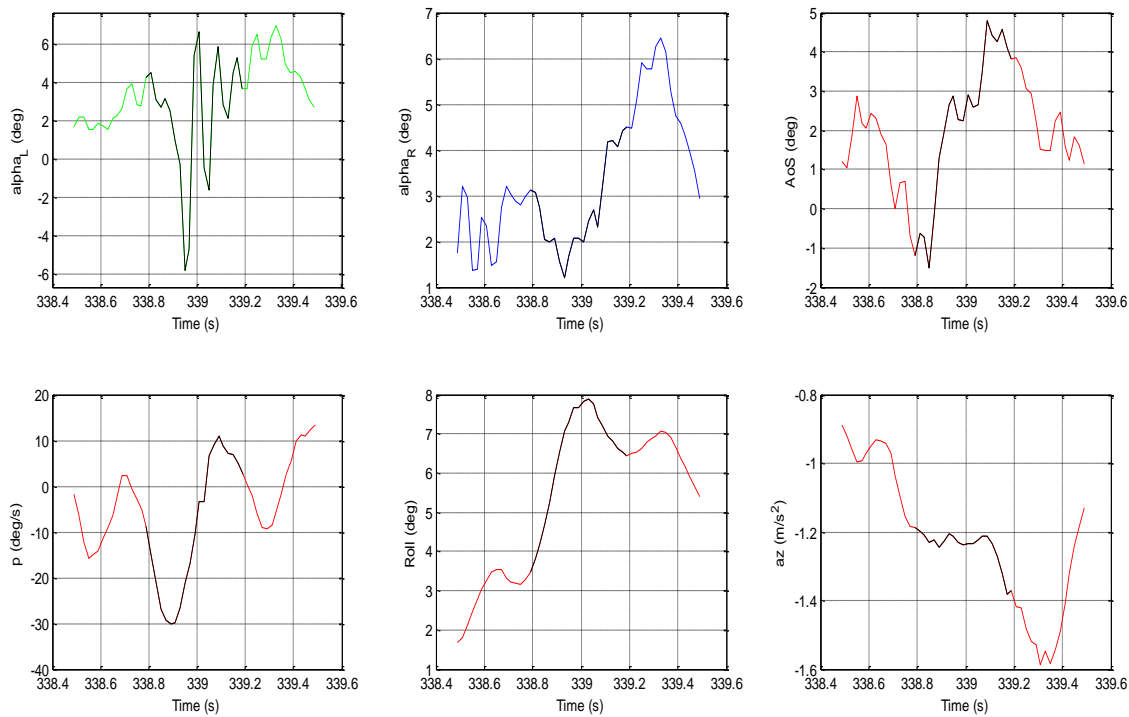


Fig. 4. Wake encounter 1 from flight 1.

3. Wake Encounter Modeling & Simulation

The estimation of aircraft response during wake encounter was analyzed during the project. Strip theory and vortex lattice method were used for the calculation of related aerodynamic forces and moments for Phastball UAVs during wake encounters. A Phastball UAV is shown in Fig. 5 with its geometry information shown in Table 2.



Fig. 5. WVU Phastball UAV

TABLE 2 PHASTBALL FUSELAGE AND WING DIMENSIONS

Length	Height	Wingspan	Chord	Airfoil
2.21 m	0.274 m	2.23 m	0.329 m	NACA 2410

3.1 – Aerodynamic Simulation of Wake Encounter

The wake vortex generated by the leader aircraft can be modeled in different ways. In this project, the Burham-Hallock [6] wake model and Sarpkaya wake decaying model [7] are selected. Assuming that the aircraft is at steady state level flight conditions and the lift and weight are balanced, the initial vortex strength is determined by the flying speed and wingspan:

$$\rho \Gamma_0 b_0 W_L = G_{leader} \quad (1)$$

where Γ_0 is the initial circulation and b_0 is the initial vortex spacing. The wake vortex then decays and descends. Under a turbulent atmosphere with neutral stratification, the circulation decay of aircraft wake vortex in atmospheric turbulence follows [8]

$$\frac{\Gamma}{\Gamma_0} = \exp\left(-C \frac{t \Gamma_0}{2\pi b_0^2 T_c^*}\right) \quad (2)$$

where C is a constant and T_c^* is defined as

$$\varepsilon^* (T_c^*)^{4/3} = 0.7475 \quad (3)$$

where

$$\varepsilon^* = \frac{2\pi b_0}{\Gamma_0} (\varepsilon b_0)^{1/3} \quad (4)$$

The descent height can be estimated as

$$\Delta h \approx \frac{\Gamma_0 t}{2\pi \times 0.8 b_0} \quad (5)$$

A. Strip Theory

The rolling moment coefficient calculation using the strip theory has been verified with the wind tunnel measurement data in [9]. Since we have the wake vortex velocity field from the wake vortex model, the induced rolling moment coefficient on an aircraft that flies through the wake can be calculated [10]. Considering the aircraft with a wing span of $2S_F$ and flying speed W_F , and assuming that the lift slope $\partial C_{LF}/\partial\alpha$ is approximately constant in the range of small angle of attack α , we have:

$$\Gamma_F(x_F) = \frac{1}{2} W_F \Delta\alpha \frac{\partial C_{LF}}{\partial\alpha} \cdot c_F(x_F) \quad (6)$$

Since

$$\Delta\alpha \approx \frac{v}{W_F} \quad (7)$$

where v is the vertical velocity component along the spanwise direction of the wing produced by the incoming wake vortex system, we have

$$\Gamma_F(x_F) = \frac{1}{2} v(x_F) \frac{\partial C_{LF}}{\partial\alpha} c_F(x_F) \quad (8)$$

Following Eq. (8), the induced lift and momentum coefficients are, respectively:

$$C_{LF} = \frac{L_F}{\frac{1}{2} \rho W_F^2 S_F} = \frac{\partial C_{LF}}{\partial\alpha} \cdot \frac{1}{W_F S_F} \int_{-S_F}^{S_F} v(x_F) c_F(x_F) dx_F \quad (9)$$

$$C_{RF} = \frac{M_{RF}}{\frac{1}{2} \rho W_F^2 S_F \cdot 2S_F} = \frac{\partial C_{LF}}{\partial\alpha} \cdot \frac{1}{W_F S_F \cdot 2S_F} \int_{-S_F}^{S_F} v(x_F) c_F(x_F) x_F dx_F$$

where S_F is the plan form area defined as

$$S_F = 2S_F \bar{c}_F \quad (10)$$

with \bar{c}_F equal to the average chord length of the wing.

The velocity distribution of a wake vortex can be modeled, simulated, or measured. As mentioned, we use a vortex model following the Burnham-Hallock vortex [6]

$$v = \frac{\Gamma}{2\pi} \frac{r}{r_c^2 + r^2} \quad (11)$$

where r is the distance from an arbitrary point to the vortex center, r_c is the vortex core radius, and Γ is the vortex strength.

B. Vortex Lattice Method

The vortex lattice method used in this study consists of representing the wing and other parts of the aircraft with a finite rectangular array of horseshoe vortices. The strengths of the horseshoe vortices are determined by velocity boundary conditions on the surface of the aircraft parts in inviscid fluid flow, i.e., the impermeable boundary condition for the velocity. Each horseshoe

vortex crosses the panel in the quarter chord line and then goes back to infinity behind the wing. The infinite vortex line induces a flow field around a line with the induced flow perpendicular to the radius and the strength inversely proportional to the radius, according to Boit-Savart law. The field is represented by the equation:

$$\mathbf{U}_j = \sum_i^n \frac{\Gamma_i}{2\pi \cdot r_i} \mathbf{j} = 1, 2 \dots n \quad (12)$$

where Γ_i is the horseshoe vortex strength, r the distance of the field location to the horseshoe vortex line, and U the induced velocity. The mathematical model is composed of a set of vortex lines arranged in a horseshoe pattern. Each horseshoe vortex starts at infinity behind the wing and moves forward to one of the subdivisions of the wing (called the panel). The flow field from all the vortices creates a downwash on the panel. This induced flow should be balanced out by the boundary condition set by the free stream and the angle of attack. It is then possible to solve for vortex strength. Once Γ_i is known, the force on the panel can be calculated as:

$$\mathbf{F}_i = \rho_\infty V_\infty \Gamma_i \cdot l \quad (13)$$

where \mathbf{F}_i is the force vector, ρ the air density, V_∞ the air velocity, and l the length or span of the vortex segment crossing the panel. By adding all the panels together, the resultant force is finally calculated as:

$$\mathbf{F} = \rho_\infty V_\infty \sum_{i=1}^n \Gamma_i \cdot l \quad (14)$$

The vortex lattice method allows for an arbitrary number of panels to be used to create a system of equations.

C. Simulation of a Phastball UAV in Wake Vortex

The advantage of the vortex lattice method is that it can simulate not only the main wing but also the fuselage and the tail so that the rolling moment coefficient of the entire aircraft can be calculated. Fig. 6 shows the Phastball UAV model and the mesh built in the vortex lattice method. The main portion of the Phastball wing features a NACA 2410 airfoil and is made up of three sections: an inboard section and two outboard sections (including winglets). The NACA 0009 was used for both the horizontal and vertical stabilizers. The control surfaces on Phastball include two elevators, two ailerons, and a rudder. More details of the UAV can be found in [3].

During formation flight simulation, the distance between the two UAVs is 12 m, the flying speed is 30 m/s, and the weight of each UAV is 110/ N, which matched real flight experiments [11]. The steady state angle of attack is 2 degrees. The two UAVs fly at the same altitude during the simulation. According to Eq. (1), the strength of the vortex induced by the leader is 5.4 m²/s. It then decays to 5.25 m²/s at 12 meters behind the leader calculated by Eqs. (2)-(4) with the constant $C = 0.45$ in Eq. (2) for this case. Because the time for vortex decay is only 0.4s based on the separation distance and flying speed of the UAV formation, the vortex does not decay much. A pair of vortices, with the above strength and a 0.2 m core size, is placed at the wing span-wise location of the follower. Fig. 7 shows the result of the analysis when putting the vortex center on the main wing. The rolling moment coefficient has different values with different locations of the center of the vortex pair relative to the center of the fuselage. It shows that at the center of the fuselage (i.e., location 0), the induced rolling moment coefficient is zero. That means the two vortices in the vortex pair are located symmetrically with respect to the center of the UAV. Each

one is close to the wingtip of the UAV. Therefore, the rolling moment caused by one is canceled by the other. The maximum rolling moment coefficient occurs when the vortex pair location is -0.8 half wingspan, i.e., when one vortex is at the center and the other one is at -1.6 half wing span. It is known for a single vortex, it creates the greatest rolling moment coefficient at the center. As the other vortex is located at -1.6 half wingspan, the counter effect is small enough to be neglected since it is relatively far away from the main wing. Hence, it is still the worst case when one vortex of the wake vortex pair is at the center of the following UAV.

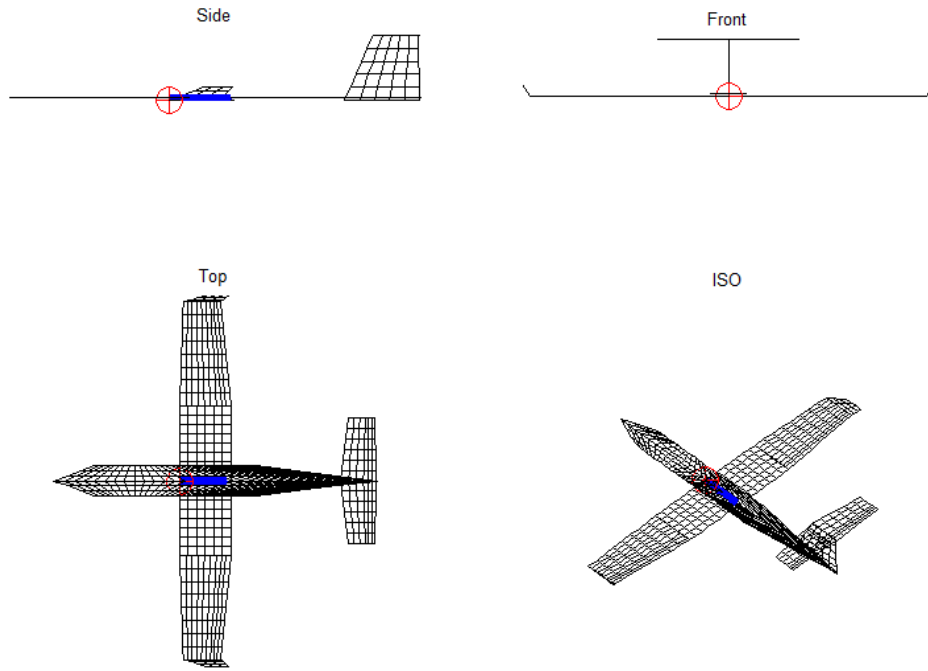


Fig. 6. Vortex lattice mesh of the UAV.

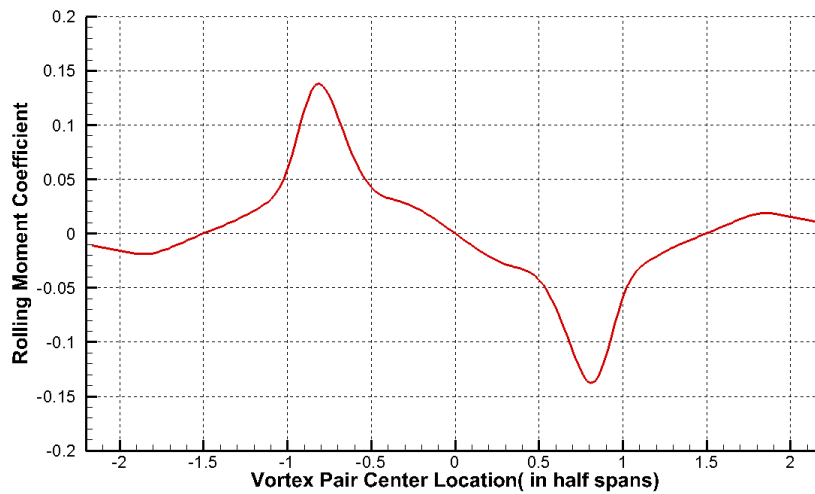


Fig. 7. Rolling moment coefficient for different vortex pair locations relative to the UAV fuselage in the unit of meter (along wingspan).

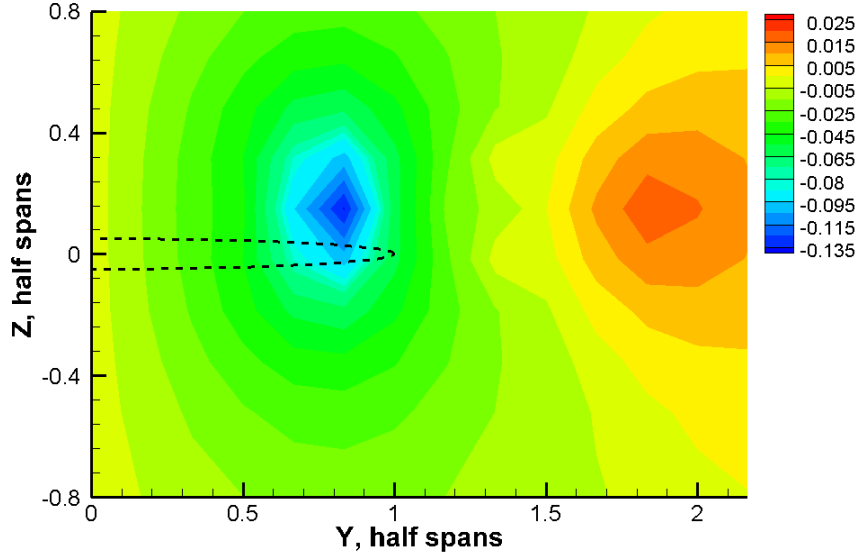


Fig. 8. Rolling moment coefficient for different vortex pair locations relative to the following UAV fuselage in the unit of half wingspan (view from tail).

Fig. 8 shows the result of the rolling moment coefficient analysis when the field of view is expanded to 2D; also, the descent distance expressed in Eq. (5) was considered. The dotted line represents the location of the half main wing of the follower. The contour levels represent the rolling moment coefficient values at the location where the leader location is relative to the follower. Same as shown in Fig. 7, the worst position in term of potential roll hazards when the strongest induced rolling moment coefficient occurs is at around 0.8 half wingspan. Table 3 compares the forces of this worst case with those without a wake vortex encounter. The wind forces are in the wind coordinate system and the body force is in the body frame of reference. Because of the 2-degree angle of attack in this case, the two coordinate systems are slightly different. When the following UAV flies through the wake vortex pair, there is also a large amount of pitch and yaw moments because of the angle of attack. This should also be considered as a hazardous situation for the UAV. The net body and wind forces indicate that the UAV undergoes much of the forces at the same time when the induced rolling moment is the highest, or worst.

Fig. 9 shows the result of the induced lift coefficient analysis for the wake encounter. The lift coefficient (C_L) varies when the location of the center of the vortex pair changes relative to the center of the follower fuselage. It shows that at the location of 1.8 half wingspan in the span-wise (Y) direction and about 0.2 half wingspan in the vertical (Z) direction, where the induced rolling moment is not the strongest in Fig. 8, an optimal value of lift coefficient is achieved. That is, the induced C_L is at maximum. This means when the leader and follower wings overlap about 20 percent of the wingspan, the follower can benefit significantly from the wake encounter for the lift.

The wake vortices also affect the drag coefficient. Fig. 10 shows the results of the total drag coefficient analysis for the wake encounter. Specifically, the analysis of the results shows that at the location of 1.8 half wingspan in the span-wise (Y) direction and about 0.2 half span in the vertical direction, coincidentally the same location of the optimal value of C_L in Fig. 9, the lowest value of C_D is achieved. This means when the leader and follower wings overlap about 20 percent of the wingspan, the follower can benefit not only from increased lift, but also from reduced drag.

This “sweet spot” is identified for the same type of aircraft in a static sense [10], while several different aircraft types were also discussed in [10].

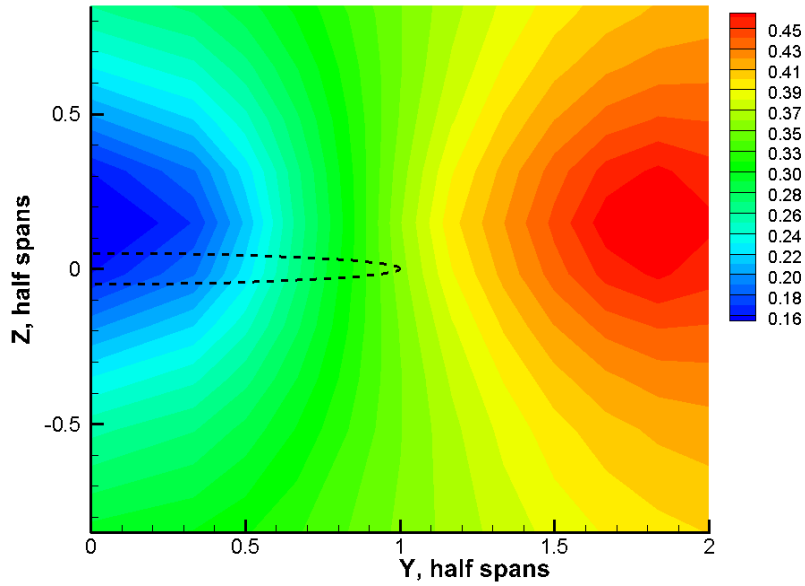


Fig. 9. Lift coefficient contours, with the same relative locations as in Fig. 8.

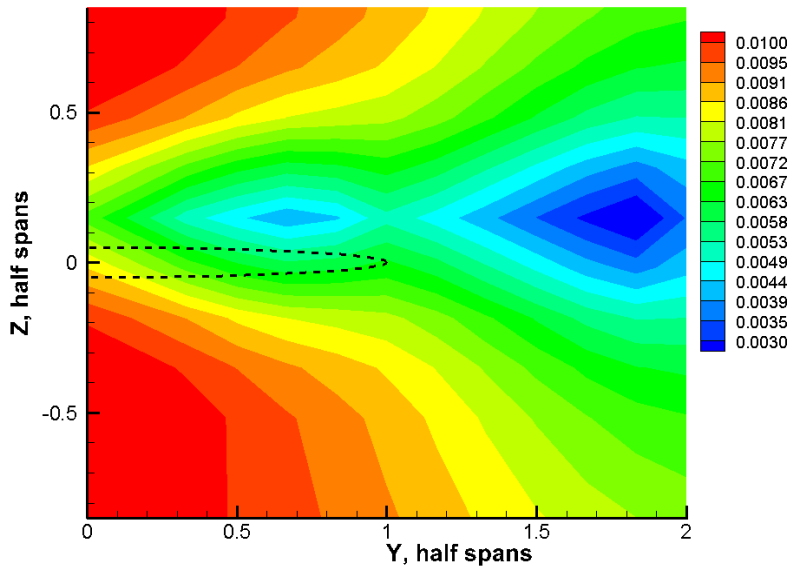


Fig. 10. Drag coefficient contours, with the same relative locations as in Fig. 8

TABLE 3. NET FORCE RESULTS FROM THE VORTEX LATTICE METHOD

	Net wind force (N) (with/without wake)		Net body force (N) (with/without wake)		Net body moments (Nm) (with/without wake)
Drag	3296/0.9189	X	3301/5.103	Roll	183.9/1.6e-13
Side	-436.2/-1.31e-12	Y	-436.2/-1.31e-12	Pitch	-370.6/-23.14
Lift	-202.7/172.5	Z	-87.54/172.4	Yaw	-531.8/-1.6e-12

3.2 – Aerodynamic & Flight Dynamic Simulation of Wake Encounter

The wake encounter simulation platform, named HawkWakeSim, is developed under MATLAB Simulink®, which is an integration of flight dynamics and aerodynamics simulations. The flight dynamic simulator used in this research is developed based on the one introduced in Beard’s book [12]. The simulation code calculates forces, moments, as well as aircraft dynamics given the aerodynamics coefficients and aircraft initial conditions. The Tornado software [13] is used as the starting point for aerodynamics simulation purpose. Tornado is an open source aerodynamic software implemented in MATLAB using a vortex lattice method. It can calculate the aerodynamic coefficients given the aircraft geometry and flight conditions. The developed wake encounter simulation platform can simulate different wake encounter scenarios and visualize wake induced oscillations. It is also capable of simulating wake encounters during leader-follower close formation flight. The simulation model built under Simulink is shown in Fig. 11, which illustrates how the aerodynamic simulation has been integrated with the flight dynamics simulator. HawkWakeSim can simulate different wake encounter scenarios including different leader aircraft and visualize wake induced oscillations. It is also capable of simulating wake encounters during leader-follower close formation flight. The system diagram for HawkWakeSim is provided in Fig. 12, which illustrates how the aerodynamic simulator is integrated with the flight dynamics simulator.

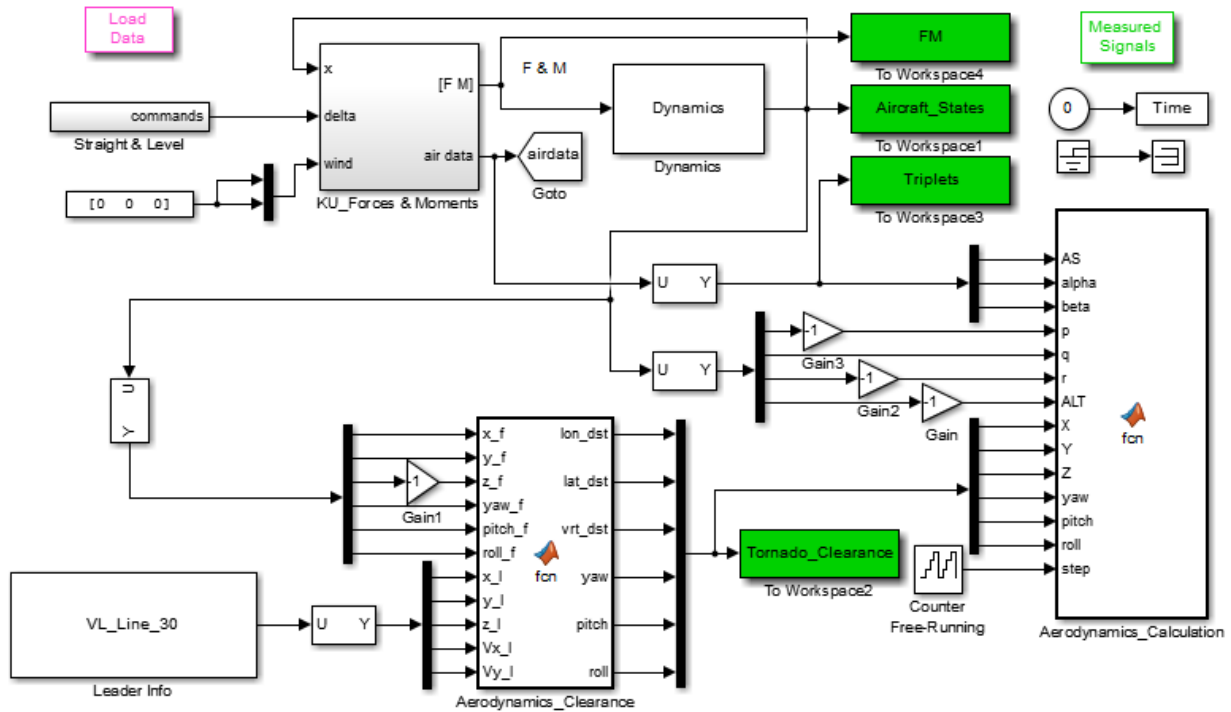


Fig. 11. Wake encounter aerodynamics and flight dynamics simulation platform.

Wake encounter simulation results presented here are generated through the implementation of a virtual leader aircraft, which is designed to fly at steady state. Meanwhile, the follower aircraft is trimmed to fly at similar nominal situations with a different heading angle in order to simulate lateral cut through, also known as lateral wake crossing. At each time step, aerodynamic coefficients of the follower aircraft, such as lift and rolling moment coefficients are first updated

in the flight dynamics simulator. These coefficients are calculated by the aerodynamics simulator at given conditions. Then, the states of the follower aircraft, including aircraft triplets $[V \alpha \beta]$, attitudes $[\phi \theta \psi]$, positions $[p_n p_e p_d]$, accelerations $[a_x a_y a_z]$, rotation rates $[p q r]$, are updated based on forces and moments calculated from the flight dynamics simulator. In order to achieve the seamless integration of aerodynamics and flight dynamics simulation under MATLAB Simulink, Tornado software was modified so that it can run automatically during the simulation process. It is worth mentioning that the wake induced oscillations are considered in the aerodynamic coefficients calculated out from aerodynamics simulation program. These coefficients are then updated in the flight dynamics simulation for forces, moments and aircraft states calculation, which eventually turns into the attitude and position information of the follower aircraft under the influence of wake vortex.

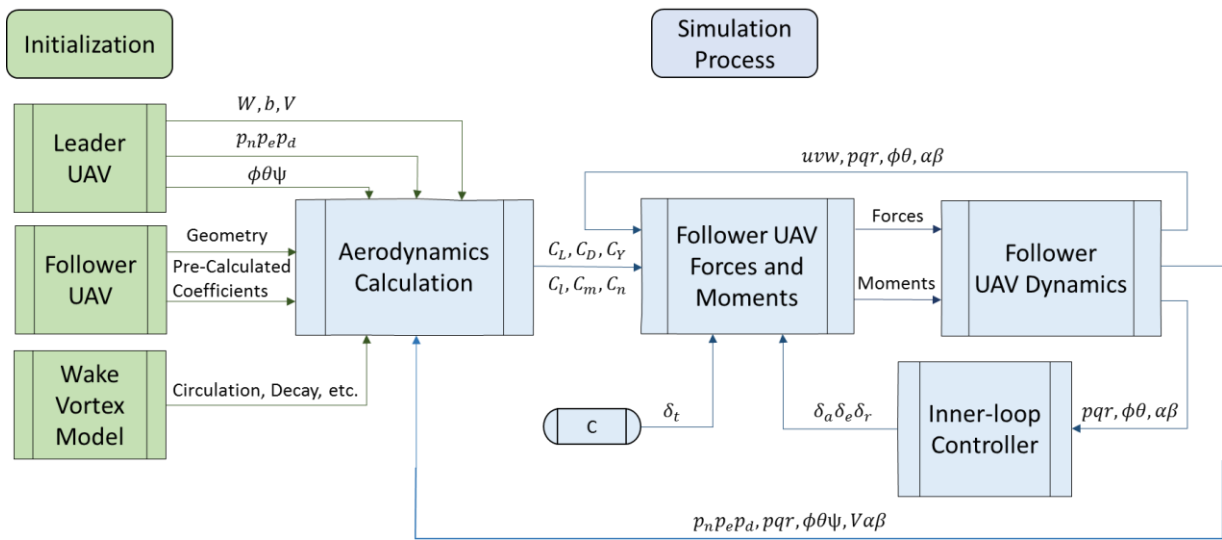


Fig. 12. System diagram for wake encounter simulator with inner-loop controller setting.

A. Simulation Results

In the following section, simulation results from wake encounters with different formation clearance and lateral encounter angles are presented and discussed. During the simulation, both leader and follower aircraft maintain the control commands which are trimmed at 31 m/s air speed based on aerodynamic initial coefficients calculated by HawkWakeSim.

Wake encounter with a 90 degrees lateral encounter angle is tested. In this test, the follower aircraft is commanded to cut through both vortex cores generated by the leader aircraft. In this simulation, the leader is flying from south to north and the follower is flying from west to east, both at an altitude of 100 meters. The follower is designed to cut through the vortex cores at 12 meters behind the leader aircraft.

It can be seen from Fig. 13 that the inertial AOA of the follower aircraft changed about 2 degrees during the wake encounter. Inertial AOA is defined as AOA estimates obtained from inertial sensors such as accelerometers. On the contrary, local AOA is defined as local flows directly measured by flow angle sensors including multi-hole Pitot tube or flow vanes. With the nominal condition of 0.3 degree, the inertial AOA drops slightly below 0 degree and bounces back to 1.7 degrees. However, the local AOA changed at a much larger magnitude. The difference

between the inertial AOA and local AOA during the wake encounter is caused by the local flow of the wake vortex. Since it is a wake encounter with 90 degrees lateral encounter angle, wake induced oscillations should also be observed from a_z and q . Results shown in Fig. 14 and Fig. 15 are as expected, with a_z changes with a magnitude of 1.1 G and q changes with a maximum magnitude of about 10 degrees/ second.

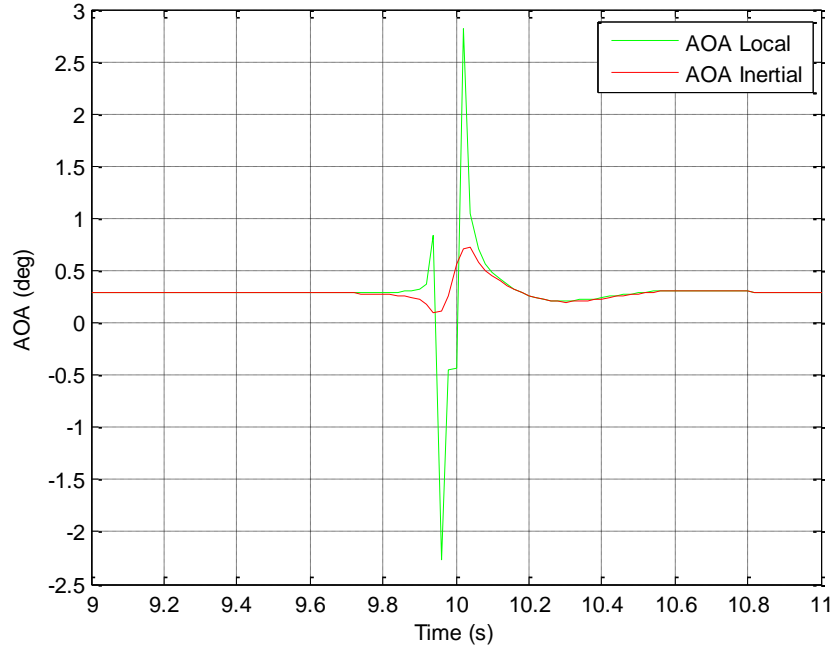


Fig. 13. AOA of the follower aircraft during wake encounter with 90 degrees lateral encounter angle.

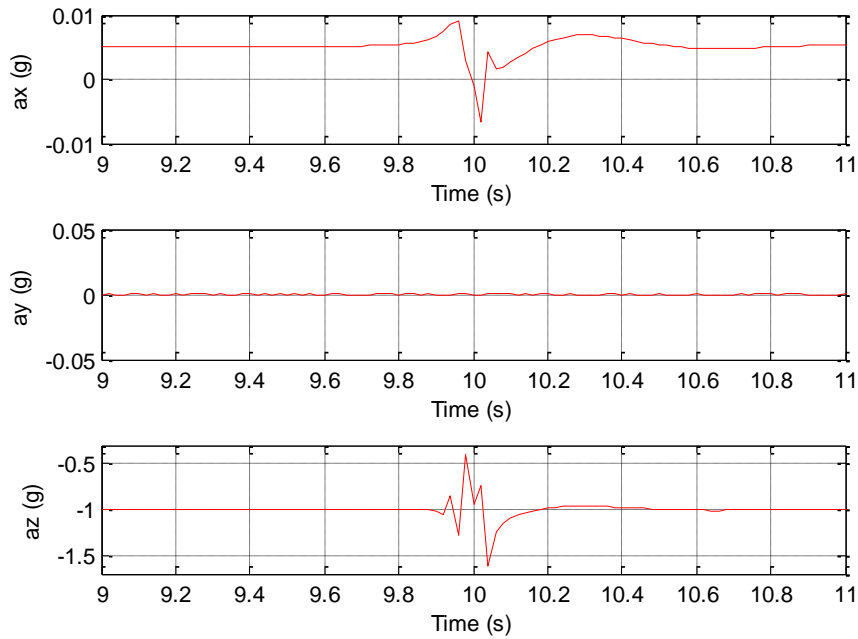


Fig. 14. Accelerations of the follower during wake encounter with 90 degrees lateral encounter angle.

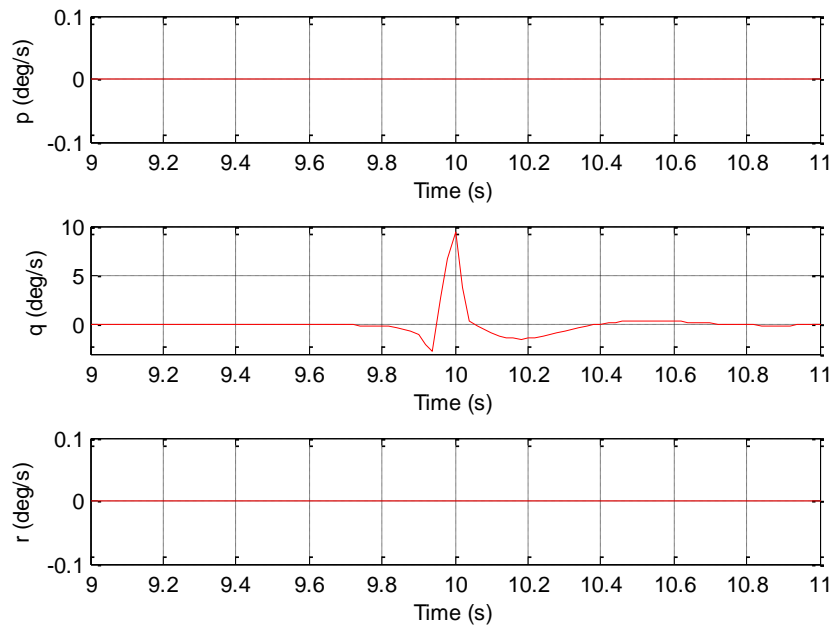


Fig. 15. Rotation rates of the follower during wake encounter with 90 degrees lateral encounter angle.

B. Cross Validation with Flight Test Data

The flight test results are compared with simulated wake encounter cases. In the simulations, the follower aircraft cut through both vortex cores generated by the leader aircraft with a 30 degrees lateral encounter angle. This angle was selected to be similar to the actual flight test scenario. The flight trajectories for both simulation (left) and flight test (right) are shown in Fig. 16. The flight test trajectory is plotted based on onboard GPS data collected from both leader and follower aircraft.

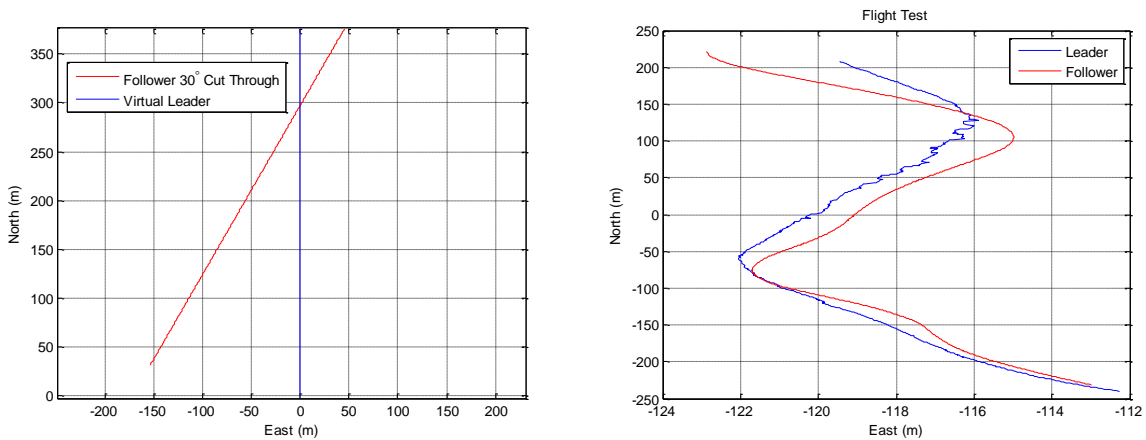


Fig. 16. Flight trajectories of wake encounter: simulation (left) and flight test (right).

A similar trend of AOA movements during the wake encounter from both simulation and flight test data can be seen in Fig. 17. The difference in magnitude may be caused by the cutting

trajectory, or the difference of wake strength, which indicates that the vortex model used in the simulation is not as strong as the real wake vortex.

Wake induced oscillations can also be observed from the simulation result a_z (with a magnitude of 1 G) as shown in the third column of the red line in Fig. 18, as well as all three rotation rates shown in Fig. 19.

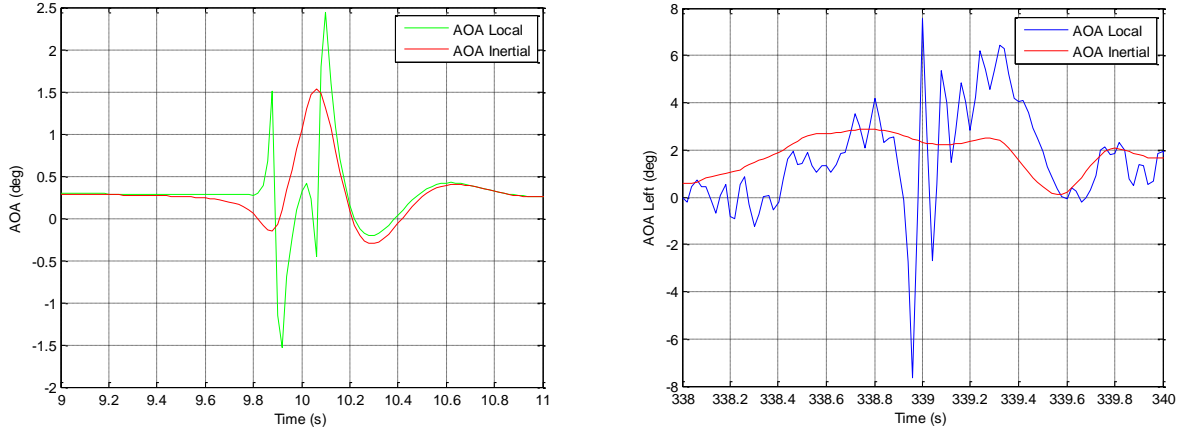


Fig. 17. AOA of the follower aircraft during wake encounter: simulation (left) and flight test (right).

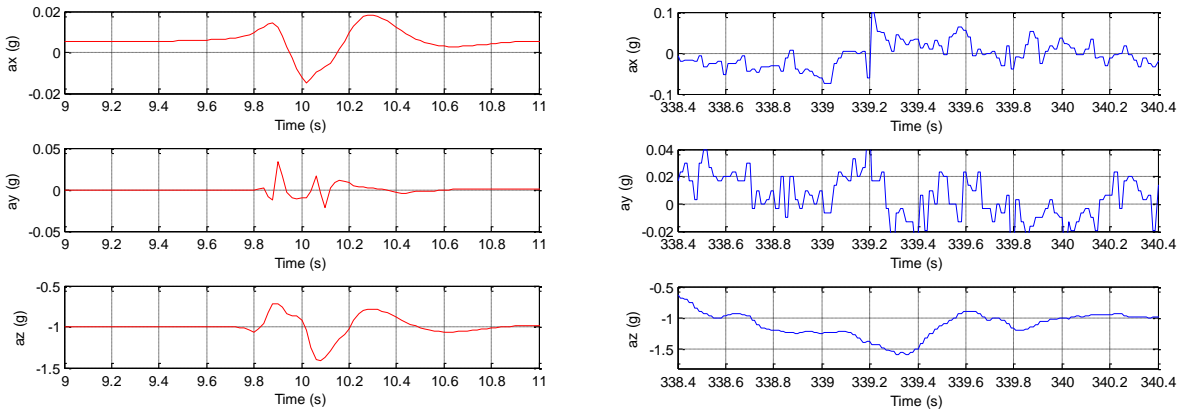


Fig. 18. Accelerations of the follower during wake encounter: simulation (left) and flight test (right).

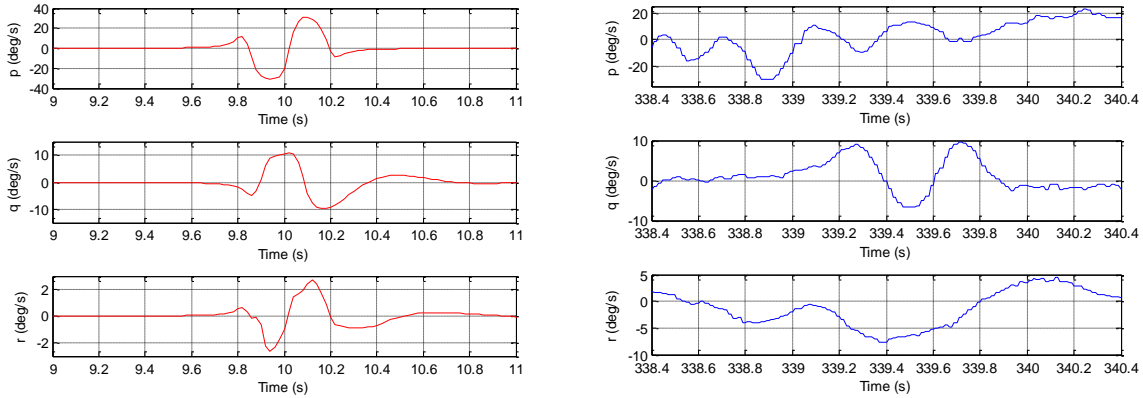


Fig. 19. Rotation rates of the follower during wake encounter: simulation (left) and flight test (right).

4. Wind Velocity Estimation

Four different nonlinear state space formulations of the wind velocity estimation problem are investigated. Each of these different formulations was considered based on the different availability of sensor information, as shown in Table 4. Since each formulation uses the wind triangle relationship [2], it is essential to have some information about both ground speed and airspeed, therefore all of the considered formulations use Pitot-static tube airspeed and GPS velocity measurements. An Inertial Measurement Unit (IMU) provides measurements of the body axis acceleration and angular rate vectors, which provides indirect information about the aircraft velocity and attitude. Angle of attack and sideslip vanes offer measurements of the relative flow angles of the aircraft which is also related to the aircraft airspeed. The details of each of these formulations are presented in [4].

TABLE 4. SENSOR INFORMATION USED IN EACH FORMULATION

Information Source	Formulation	Formulation	Formulation	Formulation
	#1	#2	#3	#4
Pitot-Static Tube	X	X	X	X
GPS Velocity (North and East)	X	X	X	X
GPS Velocity (Down)		X	X	X
IMU			X	X
Angle of Attack and Sideslip Vanes				X

4.1 – Simulation Study

A simulation study was first conducted in order to test the feasibility of the considered wind estimation formulations where an explicit truth could be used for comparison. The simulation environment proposed in [5] was used to consider the spatial variations in the local wind field. Fig. 20 shows a simulation scenario consists of the aircraft making a right turn by banking to a 60° roll angle. The estimated wind velocity is not known by the automatic controller. The resulting top-down flight trajectory is shown in Fig. 20. Using this simulated flight data set, the estimation results were calculated for each wind estimation formulation resulting in Fig. 21.

Fig. 21 shows that formulation #4 provides the closest match to the simulated wind speed components, while the other three formulations deviate from the simulation truth. Additional simulation scenarios and statistics analysis of the estimation errors can be found in [4].

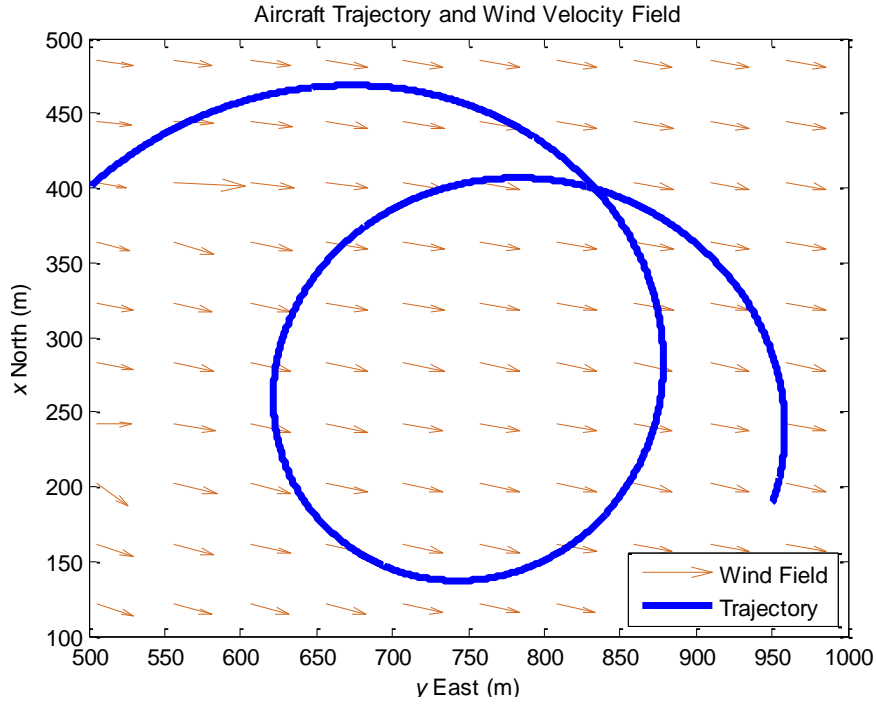


Fig. 20. Simulated flight trajectory and wind field.

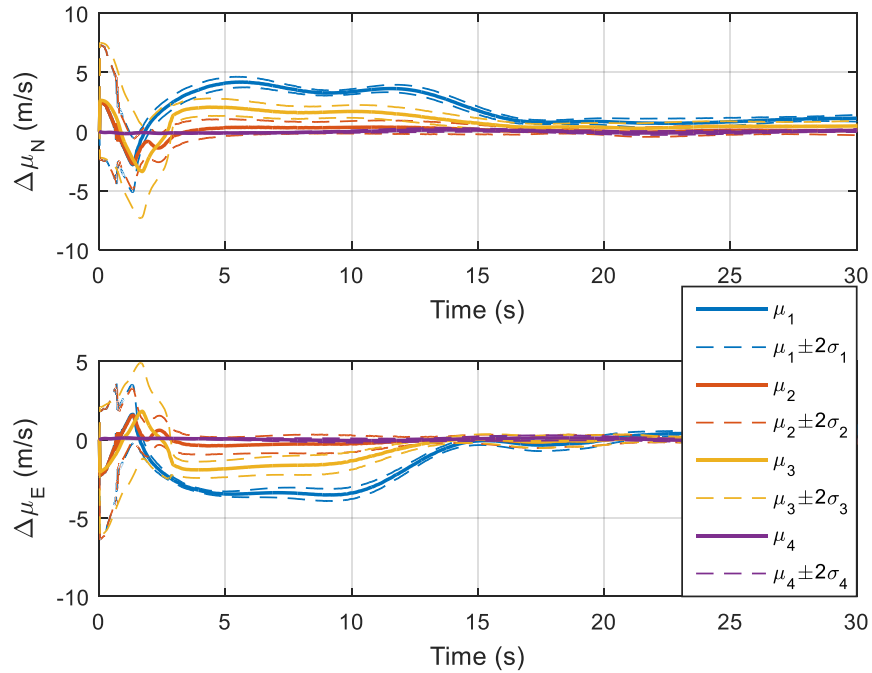


Fig. 21. Estimated wind speed components

4.2 – Validation with Flight Data

Two sets of Phastball flight data were used for validating the developed wind velocity estimation algorithms. The typical aircraft altitude during the flight is 70 m. The top-down flight trajectories from these two data sets are overlaid on a Google Earth image of the flight testing location along with the location of a local weather station in Fig. 22. As shown in Fig. 22, the

aircraft and the weather station are never at the same location, and therefore the onboard wind velocity estimates are not directly comparable to the weather station data, which can only be used for general reference purposes.



Fig. 22. Flight trajectories and weather station location, © 2014 Google.

Using the available flight data, each formulation was implemented to estimate the wind velocity components. The estimated components of wind velocity are shown in Fig. 23. It shows that formulations #1, #2, and #3 provide similar estimates for the wind speed, while formulation #4 has similar trends but differs significantly.

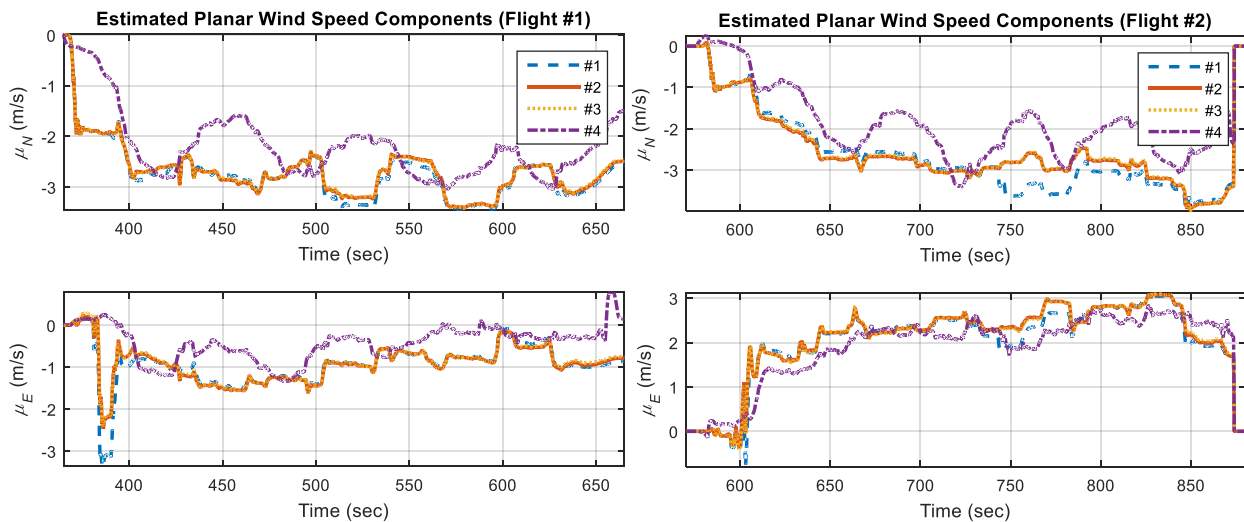


Fig. 23. Estimated planar wind speed components for flight #1 (left) and flight #1 (right).

Fig. 24 shows a comparison of the estimated total planar wind speeds are compared with the power law corrected (for compensating the ground friction effects) measurements [14, 15] from the ground weather station.

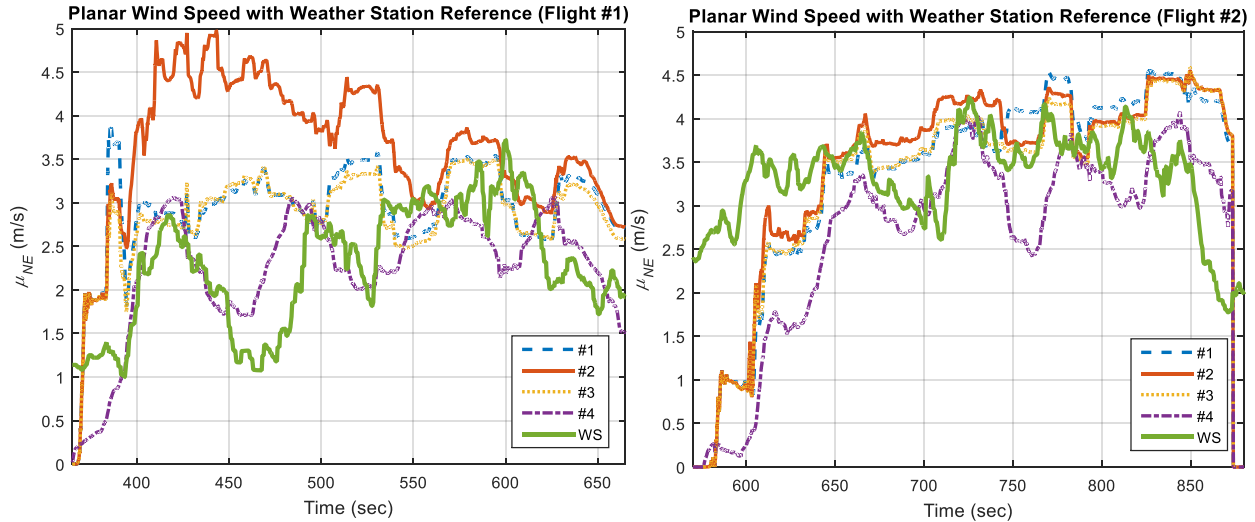


Fig. 24. Total planar wind speed with weather station reference data for flight #1 (left) and flight #1 (right).

It is shown in Fig. 24 that each formulation reasonably matches the wind speed as measured by the weather station. While none of these estimates closely match the weather station data, this is expected since the weather station was measuring speed at a different location in the local wind field, and local turbulence would cause differences between the wind speed measured at different points. However, these results are encouraging. Formulations #1, #2, and #3 offer similar results, while formulation #4 contains significant differences from the others. Formulation #4 is better able to capture some of the trends measured by the weather station data.

5. UAV Testbed Upgrade and Flight Testing

At the beginning of the Phase II of the project the research team assessed that the Gen-V avionics [16] used during the Phase I effort was no longer adequate. Therefore, a new avionics package was designed to support precision autonomous close formation flight experiments. The WVU Phastball aircraft were upgraded with new propulsion systems, Real Time Kinematic (RTK) GPS receivers (Novatel OEM615®), a nose mounted SpaceAge® mini air-data probe, two wing-mounted Aeroprobe® 5-hole pitot tubes, tufts on the wings with motions recorded by a tail camera, new communication systems (for inter-vehicle communication and for receiving the RTK correction from a ground station), and a newly designed Gen-VII avionics. Fig. 25 shows the new components on the Phastball test bed.

The Gen-VII Avionics consists of two custom Printed Circuit Boards (PCB), the Nose-board, shown in Fig. 26, and the Autopilot board, shown in Fig. 27, along with a PC-104 format single board computer processing the on-board control scheme. The Nose-board gathers and conditions data from a collection of sensors located in the front section of the aircraft, including: wind vanes for angles of attack and sideslip measurements, a Pitot tube and pressure sensors for measuring static/dynamic pressure, and a RTK GPS receiver with a RF modem for communicating with a ground station. The autopilot board interfaces directly with the single board computer and acts as a communications hub for all of the information to and from other subsystems of the aircraft. Another key feature of the autopilot board is the fault-tolerant transition between human-pilot

control from the pilot on the ground and autopilot control generated by the onboard flight control scheme.

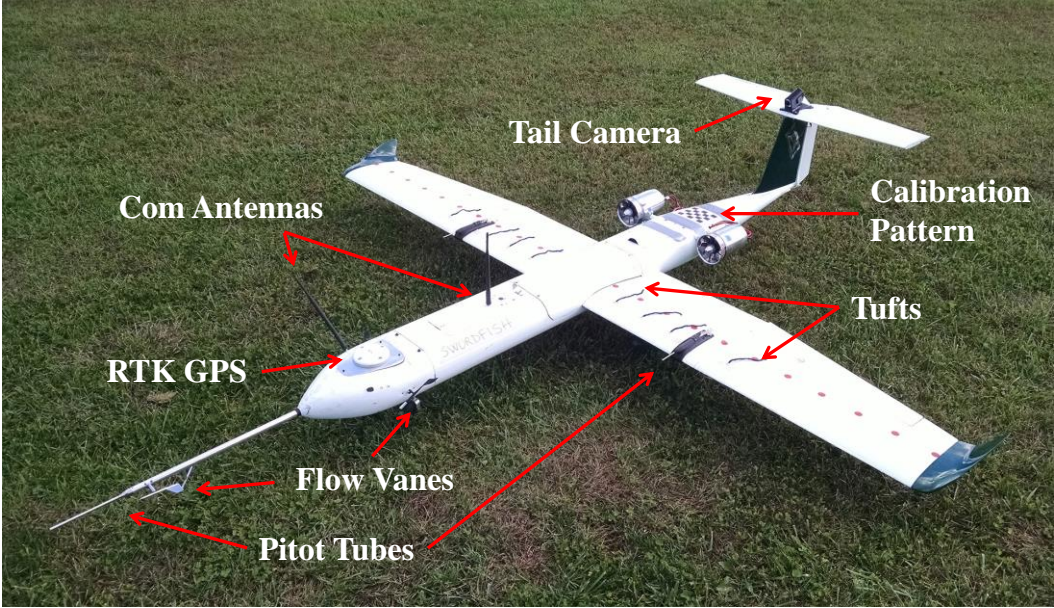


Fig. 25. Instrumentation of a Phastball Aircraft



Fig. 26. Gen-VII avionics: nose-board.

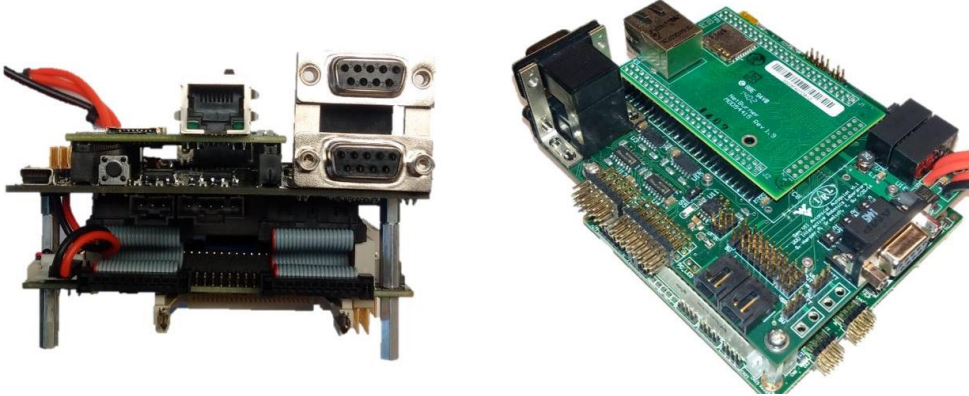


Fig. 27. Gen-VII avionics: autopilot board.

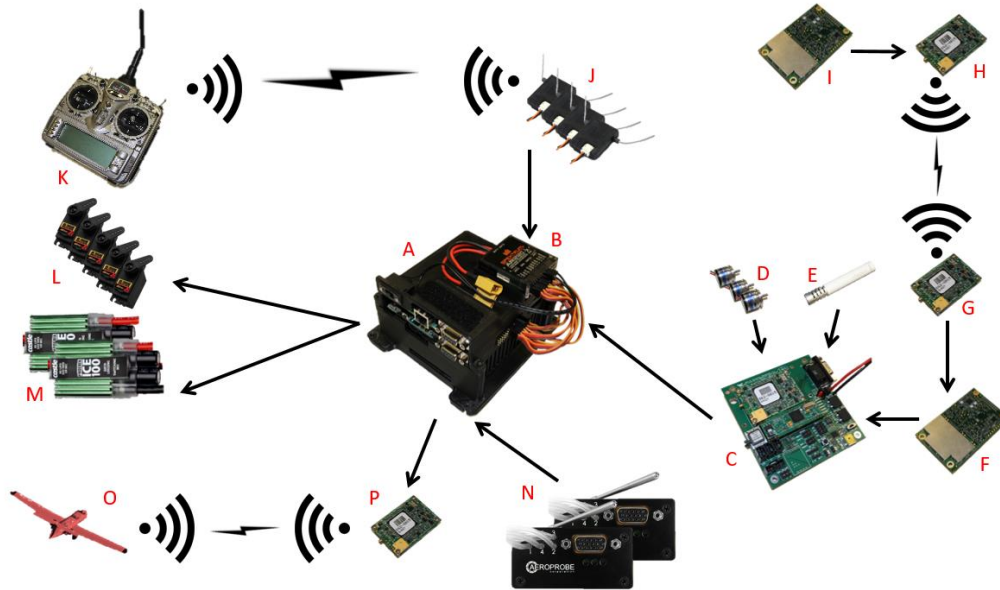


Fig. 28. Phastball electrical systems: (A) autopilot and computer in enclosure, (B) spectrum R/C receiver, (C) nose-board, (D) wind vane angle sensors, (E) temperature/humidity sensor, (F) Novatel GPS receiver, (G) RF modem receiving RTK correctors, (H) RF modem transmitting RTK correctors, (I) ground station Novatel GPS receiver, (J) spectrum receiver satellites, (K) R/C transmitter, (L) surface control servos, (M) engine speed controllers, (N) Aeroprobe micro air data system, (P) RF modem to communicate with (O) fellow aircraft(s).

The overall upgraded aircraft instrumentation is shown in Fig. 28. Alongside the main avionics, the wings were retrofitted with additional instruments for the purpose of wake detection and estimation during formation flight. Specifically, each wing is instrumented with an Aeroprobe® micro Air Data System (ADS) which provides measurements of angle of attack, angle of sideslip, airspeed, and altitude at a midpoint of the wing. The ADS utilizes a 5-port Pitot-static probe coupled with a small air data computer performing all of the calculations. Also an array of high contrasting colored yarn tufts was mounted across the wingspan and were filmed using a tail-mounted camera (Sony HDR-AS10®).

More than 45 flight experiments were performed throughout Phase II to test the avionics design and new sensors, to fine tune the formation controller, and to collect research data. Many practical challenges associated with the integration of new sensors, avionics, propulsion systems, communication devices, and flight control software were encountered and overcome during this period. However this process took longer time than expected, which prevented performing of additional precision formation flight experiments. With testbeds fully developed and validated, we plan to continue flight experiments in the near future to advance the formation flight research.

6. Relative Navigation using Inter-Aircraft Ranging

Accurate and robust real-time relative navigation is important for precision close formation flight. A novel differential GPS/INS/ranging measurement fusion algorithm was developed with a focus of yielding substantially improved robustness to error sources that are commonplace and known to degrade the performance of integer fixed Carrier Phase Differential GPS (CP-DGPS, i.e., relative RTK). The premise of taking this approach is the fact that integer fixed CP-DGPS/INS systems have already been demonstrated experimentally to offer centimeter-scale relative

navigation accuracy [17]. Therefore, this work focused on increase the robustness by enhancing the relative navigation filter’s ability to correctly and quickly fix integers phase ambiguities, despite the presence of challenging conditions. This is especially relevant for implementation on small UAV platforms due to their fast dynamics and large-bank angles which often lead to dropped satellite observations, poor satellite geometry, and/or phase breaks.

The fusion algorithm architecture is shown in Fig. 29, where three sequential estimation stages are indicated. In Stage 1, the absolute navigation state of each UAV is estimated locally by each UAV through tightly-coupling INS, GPS pseudo-range, and GPS Doppler measurements. During Stage 2, the raw carrier-phase GPS observables from UAV_A are communicated to UAV_B in order to perform double-differences; a two-way time of flight range measurement between the UAVs is obtained; and the difference between the estimated absolute 3D position solutions of UAV_A and UAV_B are subtracted to form an observation in the relative navigation filter. The estimates of Stage 2 are fed-forward to Stage 3, where the phase ambiguity are resolved to integers and the relative navigation vector is adjusted accordingly. The formulation details of each of the three stages can be found in [18].

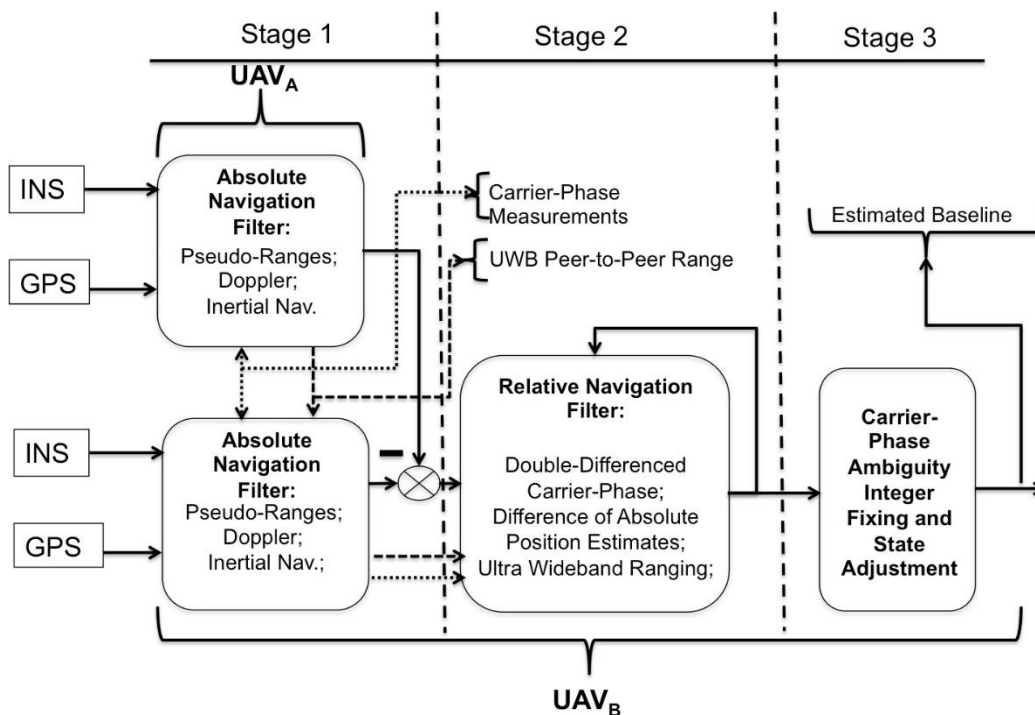


Fig. 29. Architecture for UAV relative baseline estimation (processing required for one epoch of data).

The relative navigation approach was validated with a simulation study. Fig. 30 illustrates baseline estimation performance with and without ranging radios within a Monte Carlo study. Specifically, the Cumulative Distribution Function (CDF) of the 3D Residual Sum of Squares (3DRSS) error was computed for 750 Monte Carlo simulation trials. The sensor fusion algorithm is shown to offer improved robustness for 3D relative positioning in terms of 3DRSS accuracy and increased percentage of correctly fixed phase ambiguities. Moreover, baseline estimation performance is significantly improved during periods in which differential carrier phase ambiguities are unsuccessfully fixed.

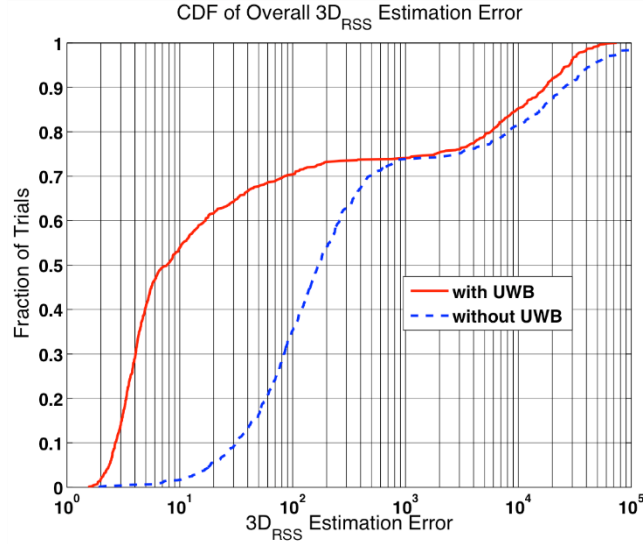


Fig. 30. CDF of the 3DRSS estimation error over the 750 Monte Carlo simulation trials, where the estimation error is evaluated over all the epochs of each flight (i.e. irrespective of being successfully fixed).

7. Computer Vision Based Tuft Angle Estimation

In this section, the method for estimating the local air flow direction on the surface of the wings using computer vision is discussed. As mentioned earlier, the Phastball UAV is outfitted with tufts attached to the surface of the wings, and the wind flow across the surface of the wings are then estimated offline from the video captured on board the flight.

The videos were captured at a 1920x1080 resolution at 30 Hz. The goal of the air flow estimation algorithm is to relate the angle of each tuft to the local air flow around the wing in the lateral direction. The estimation algorithm involves two primary steps to estimate the angle of each tuft. First, the tufts must be located in the image frame. This is done by segmenting each tuft from the image using prior information about the location of each tuft and color thresholding. Second, the orientation of each tuft must be estimated in the image frame, then the orientation must be converted from the image frame to the body frame. In this study, the camera frame is assumed to be aligned with the body frame, so the transformation between the image frame and the camera frame is not necessary. The details of the camera calibration, segmentation, and estimation algorithms are described in details in [19].

In order to evaluate the performance of the proposed approach, the results of the computer vision algorithm are compared to ADS measurements. The ADS measurements and the results from the computer vision algorithm were both offset to have zero mean on the vertical axis for comparison. The results for the left wing and right wing are presented in Fig. 31 and Fig. 32 respectively. The Root Mean Square Error (RMSE) and Mean Absolute Error (MAE) between the computer vision estimates and the ADS measurements are presented in Table 5. The tuft angles are shown to be similar to the ADS measurements, which corresponds to the angle of sideslip. Although the computer vision algorithm is not necessarily estimating the angle of sideslip, the ADS measurements provided an adequate comparison in order to validate the experiment. Additionally, tuft angle on each wing are very similar to each other, which further validate the

approach. The remaining discrepancies could be due to calibration errors, bending of the wing, or difference in the local air flow estimated by the ADSs.

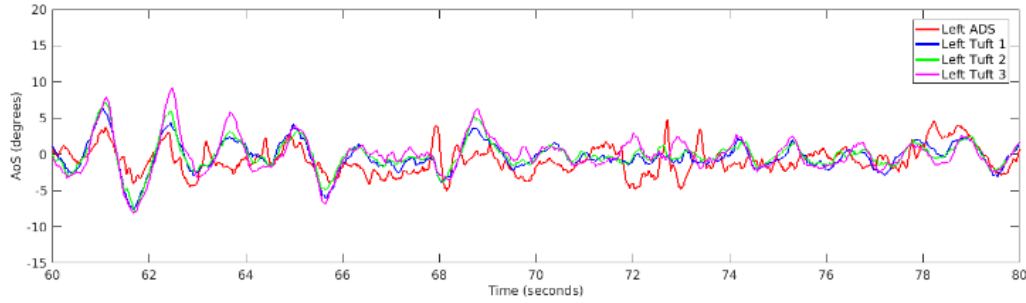


Fig. 31. Left wing comparison of the ADS measurements and the computer vision estimates of the local air flow for a 20 second flight segment.

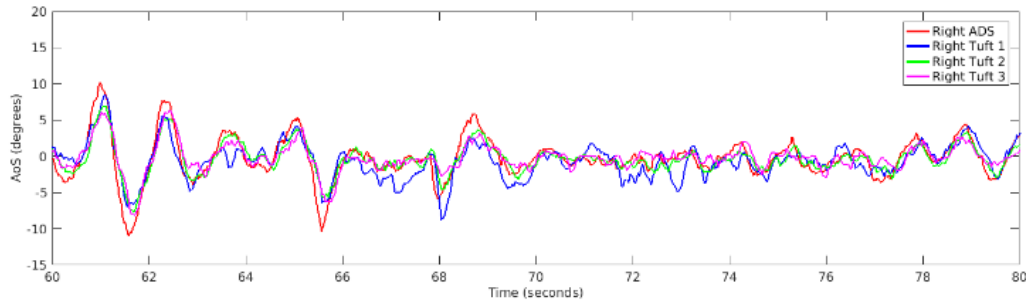


Fig. 32. Right wing comparison of the ADS measurements and the computer vision estimates of the local air flow for a 20 second flight segment.

TABLE 5: ERROR BETWEEN THE ADS MEASUREMENTS AND THE COMPUTER VISION ESTIMATES FOR THE FULL FLIGHT EXPERIMENT FOR THE LEFT AND RIGHT TUFTS

	Left Wing RMSE	Left Wing MAE	Right Wing RMSE	Left Wing MAE
Tuft 1	3.49°	2.47°	3.56°	2.58°
Tuft 2	3.62°	2.62°	1.78°	1.26°
Tuft 3	3.98°	2.92°	3.98°	1.71°

8. Conclusions

In summary, this project advanced several aspects of formation flight research in the areas of modeling, simulation, local air flow sensing, wind estimation, relative navigation, and experimental technology. During this effort, wake encounters in data collected during close formation flight experiments were identified. Wake encounter effects were observed from data collected with flow angle sensors, accelerometers, and gyroscope sensors. The wake vortex generated by the leader aircraft was modeled using Burham-Hallock wake model and Sarpkaya wake decaying model. The interaction between leader’s wake and the follower aircraft was estimated using the vortex lattice method. An aerodynamic and flight dynamic simulator for UAV

wake encounter was developed. The feasibility of using UAV test beds for wake model validation was also confirmed through the comparison of simulated and experimental results.

Four different nonlinear state space formulations of the local aircraft wind estimation problem using the UKF as the nonlinear estimator were developed. Simulation and flight testing data were used to validate wind estimation performance of each formulation.

In terms of UAV relative navigation, the benefit of incorporating peer-to-peer ranging when confronted with scenarios that typically degrade DGPS performance such as an increase level of phase breaks was characterized with the use of a Monte Carlo analysis. The ability to fix integer phase ambiguities correctly was significantly increased.

A novel method was also developed for estimating the local airflow on an aircraft's surface using computer vision based estimation of tuft angles. The estimated tuft deflections were validated through a comparison with measurements provided by two wing-mounted ADSs. These estimates can be used for wake encounter detection, wake center estimation, and stall indication.

Substantial hardware upgrades were made to the testbed aircraft, including the integration of new sensors, communication devices, propulsion systems, and a custom designed avionics system tailored for precision autonomous formation flight research. Over 45 flight experiments were performed for refining hardware design and integration, fine-tuning formation controller, and collection data to support different research efforts presented earlier. These testbeds are now ready to support more advanced formation flight experiments to be performed in the coming years.

References

- [1] Rice, C., Gu, Y., Chao, H., Larrabee, T., Gururajan, S., Napolitano, M., Mandal T., and Rhudy M., "Autonomous Close Formation Flight Control with Fixed Wing and Quadrotor Test Beds," *International Journal of Aerospace Engineering*, Volume 2016, Article ID 9517654, 2016.
- [2] McLaren, S., "Velocity Estimate Following Air Data System Failure," Master's thesis, Air Force Institute of Technology, 2008.
- [3] McGrail, A.K., "OnBoard Parameter Identification for a Small UAV", M.S. Thesis, West Virginia University, 2012.
- [4] Rhudy, M., Gu, Y., Gross, J., and Chao, H. "Onboard Wind Velocity Estimation Comparison for Unmanned Aircraft Systems," Accepted, *IEEE Transactions on Aerospace and Electronic Systems*, 2016.
- [5] Rhudy, M., "Stochastic Spatial Wind Field Simulation using a Potential Field," *AIAA Modeling and Simulation Technologies Conference*, Atlanta, GA, June 2014.
- [6] Burnham, D.C, and J.N. Hallock. "Chicago Monostatic Acoustic Vortex Sensing System, Volume IV: Wake Vortex Decay," *FAA-RD-79-103, IV*, Transportation Systems Center, 1982.
- [7] Sarpkaya, T., "New Model for Vortex Decay in the Atmosphere," *Journal of Aircraft*, Vol. 37, No. 1, 2000, pp. 53–61.
- [8] Anderson, E. A., "Experimental Study of the Structure of the Wingtip Vortex", 38th Aerospace Sciences Meeting & Exhibit, Reno, NV. 2000.

- [9] Zheng, Z. C., Ash, R. L., and Greene, G. C., “A Study of the Influence of Cross Flow on the Behavior of Aircraft Wake Vortices near the Ground,” Proceedings of the 19th Congress of the International Council of the Aeronautical Sciences, Vol. 2, pp. 1649-1659. Anaheim, CA, 1994.
- [10] Dogan, A., Venkataramanan, S., and Blake, W., “Modeling of Aerodynamic Coupling between Aircraft in Close Proximity,” Journal of Aircraft, Vol. 42, No. 4, 2005, pp. 941-955.
- [11] Chao, H., Gu, Y., Tian, P., Zheng, Z. and Napolitano, M., “Wake Vortex Detection with UAV Close Formation Flight”, AIAA Atmospheric Flight Mechanics Conference, 2015.
- [12] Beard, R. W., and McLain, T. W., Small Unmanned Aircraft: Theory and Practice, Princeton University Press, 2012.
- [13] Melin, T., “A Vortex Lattice MATLAB Implementation for Linear Aerodynamic Wing Applications,” Master thesis, Department of Aeronautics, KTH, 2002.
- [14] Cho, A., Kim, J., Lee, S., and Kee, C., “Wind Estimation and Airspeed Calibration using a UAV with a Single-Antenna GPS Receiver and Pitot Tube,” IEEE Trans. on Aerospace and Electronic Systems, Vol. 47, No. 1, Jan. 2011, pp. 109-117.
- [15] U.S. Environmental Protection Agency, “Meteorological Monitoring Guidance for Regulatory Modeling Applications,” 2000.
- [16] Gu, Y., Gross, J., Barchesky, F., Chao, H., and Napolitano, M., “Avionic Design for a Sub-Scale Fault Tolerant Flight Control Test-Bed,” Chapter 21, Recent Advances in Aircraft Technology, ISBN: 978-953-51-0150-5, pp. 499-522, 2012
- [17] Williamson, W. R., Abdel-Hafez, M. F., Rhee, I., Song, E.-J., Wolfe, J. D., Chichka, D. F., and Speyer, J. L. “An Instrumentation System Applied to Formation Flight,” Control Systems Technology, IEEE Transactions on, vol. 15, no. 1, pp. 75–85, 2007.
- [18] Gross, J., Gu, Y., and Rhudy, M., “Robust UAV Relative Navigation with DGPS, INS, and Peer-to-Peer Radio Ranging,” IEEE Transactions on Automation Science and Engineering, Volume 12, Issue 3, Jan 2015.
- [19] Strader, J., Harper, S., Gu, Y., “Aircraft Instrumentation and Computer Vision-Aided Flight Analysis of Local Air Flow,” AIAA Aviation 2016, Washington DC, June, 2016.

Appendix A. Publications from the Project

Journal Publications:

1. Rhudy, M., Gu, Y., Gross, J., and Chao, H. "Onboard Wind Velocity Estimation Comparison for Unmanned Aircraft Systems," Accepted, IEEE Transactions on Aerospace and Electronic Systems, 2016.
2. Rice, C., Gu, Y., Chao, H., Larrabee, T., Gururajan, S., Napolitano, M., Mandal T., and Rhudy M., "Autonomous Close Formation Flight Control with Fixed Wing and Quadrotor Test Beds," International Journal of Aerospace Engineering, Volume 2016, Article ID 9517654, 2016.
3. Rhudy, M., Fravolini, M.L., Gu, Y., Napolitano, M., Gururajan, S., and Chao H., "Aircraft Model Independent Airspeed Estimation without Pitot Tube Measurements," IEEE Transactions on Aerospace and Electronic Systems, 51(3):1980-95, Jul. 2015.
4. Gross, J., Gu, Y., and Rhudy, M., "Robust UAV Relative Navigation with DGPS, INS, and Peer-to-Peer Radio Ranging," IEEE Transactions on Automation Science and Engineering, Volume 12, Issue 3, Jan 2015.

Conference Publications:

1. Tian, P., He, A., Chao, H., Zheng, Z., and Gu, Y., "Wake Encounter Simulation and Flight Validation with UAV Close Formation Flight," Accepted, AIAA Guidance, Navigation, and Control Conference, Dallas, TX, Jan 2017.
2. He, A., Tian, P., Zheng, Z., Chao, H., and Gu, Y., "A Study on Wake Turbulence Encounter during UAV Formation Flight Using Coupled Aerodynamics/Flight Dynamics Simulation," AIAA Atmospheric and Space Environment Conference, Washington DC, Jun 2016.
3. Strader, J., Harper, S., Gu, Y., "Aircraft Instrumentation and Computer Vision-Aided Flight Analysis of Local Air Flow," AIAA Aviation 2016, Washington DC, Jun 2016.
4. Tian, P., Chao, H., Gu, Y., Hagerott, S., "UAV Flight Test Evaluation of Fusion Algorithms for Estimation of Angle of Attack and Sideslip Angle" AIAA SciTech Conference, San Diego, CA, Jan 2016.
5. He, A., and Zheng, Z., "Aerodynamic Simulation of Wake Encounter for Aircraft Close Formation Operations," AIAA Atmospheric and Space Environment Conference, Dallas, TX, Jun 2015.
6. Chao, H., Gu, Y., Tian, P., Zheng, C., Napolitano, M., "Wake Vortex Detection with UAV Close Formation Flight," AIAA Atmospheric Flight Mechanics Conference, Kissimmee, FL, Jan 2015.